

Calculating the representative elementary volume of porosity using X-ray computed tomography: Boda Claystone Formation core sample/Hungary

Saja M. Abutaha¹, János Geiger¹, Sándor Gulyás¹ & Ferenc Fedor²

¹University of Szeged, Department of Geology and Paleontology, Egyetem utca 2-6, 6722 Szeged, Hungary; sajaabutaha@geo.u-szeged.hu, matska@geo.u-szeged.hu, gulyas.sandor@geo.u-szeged.hu

²GEOCHEM Ltd, 55/1 Viola Str, 7761 Kozármisleny, Hungary; fedor.ferenc@geochem-ltd.eu

AGEOS

Abstract: The main objective of this study is to calculate the representative elementary volume (REV) according to voxels' porosity. Physical properties of rock-forming components of a 5 m-long core sample of the Boda Claystone Formation (BCF) were acquired using 3D X-ray computed tomography images. The REV calculation was established using the Autoregressive Integrated Moving Average, Statistical Process Control (ARIMA SPC) technique. This method (ARIMA SPC) was five times iterated by varying positions of starting voxel volume in the core sample: upper left, upper right, lower left, lower right, and middle. The general average range of REV values was from 16.56 cm³ to 46.26 cm³. Monte Carlo simulation with 1,000 runs was used to simulate the long-run properties of REV and the normalized REV of voxel-porosity. The simulated REV values were 64.80 cm³ in the upper left position, 61.44 cm³ for the upper right, 55.59 cm³ for the lower right, 53.77 cm³ for the lower left, and 42.23 cm³ for the middle. According to the simulation of the normalised REVs, their volume percentages were as follows: 40 % for the upper left, 41.34 % in the lower right, 23.86 % for the lower left. Lastly, the upper right and the central (middle) positions had almost the same percentage volumes around 15.5 %. As the initial volume started from any core sample's corners, the REV porosity range would be between 2.47 % and 2.58 %, which is close to the average voxel porosity of BCF (2.55%). However, a deviant (higher) REV porosity value was attained from the centre initiated volume (~2.8 %). Therefore, the middle part of the studied core sample might not be adequate to be considered as an initial voxel volume of the REV calculation.

Key words: Hounsfield unit (HU), voxel porosity, Autoregressive Integrated Moving Averages (ARIMA), Statistical Process Control (SPC), representative elementary volume (REV)

1. INTRODUCTION

Petrophysics is the study of the physical and chemical properties of rocks and their contained fluids (Tiab & Donaldson, 1996). Many petrophysical properties depend on the distribution of other properties such as mineralogy, pore size, or sedimentary fabric, and the chemical and physical properties of both the solids and fluids. Accordingly, petrophysical properties can be fairly constant throughout a homogeneous reservoir or vary significantly from one location to another in an inhomogeneous or heterogeneous reservoir (Fitch et al., 2015). The scale of observation is a fundamental aspect in modelling material behaviour or deriving its effective parameters from the constituent relations governed by the spatial distribution of its components. Frazer et al. (2005) commented that heterogeneity is an inherent, ubiquitous, and critical property that is strongly dependent on scales of observation and the methods of measurement used. Frazer et al. (2005) and Fitch et al. (2015) suggest that heterogeneity does not necessarily refer to the overall system, or individual rock/reservoir unit, but instead may be dealt with separately for individual units, properties, parameters, and measurement types. Recently, accurate determination of rock heterogeneity becomes essential for a variety of industrial

applications. For instance, it plays a crucial role in determining the reservoir's ability to recover oil and gas (Russo & Jury, 1987; Chang & Gao, 1995; Muhlhaus & Oka, 1996; Webster, 2000), carbon geo-storage efficiency (Feyel & Chaboche, 2000; Peerlings & Fleck, 2001; Kouznetsova et al., 2001, 2002), contaminant mitigation and natural source zone depletion (Bear & Bachmat, 1990; Clausnitzer & Hopmans, 1999), water discharge and extraction rates (Brown et al., 2000; Baveye et al., 2002) or geothermal energy production feasibility (e. g., Al-Raoush & Willson, 2005). It is thus important to understand rock heterogeneity in detail to make reliable predictions or process optimization. The issue of how the scale of measurement will be impacted by heterogeneity can be represented through the concept of a Representative Elementary Volume (REV) to characterise the point when increasing the size of data population no longer impacts the average, or upscaled, the value obtained (Bear, 1972; Bachmat & Bear, 1987).

One of the simplest techniques to determine REV was proposed by Bear (1972); it evolved from plotting porosity against rock volume, the point at which the parameter, i.e., porosity, becomes constant identifies the REV. Almost all recent REV studies have evaluated the variation of X-ray imaged porosity with increasing measurement volumes. Such studies have been

carried out for glass bead mixtures (Al-Raoush & Willson, 2005; Clausnitzer & Hopmans, 1999), rocks (Biswal et al., 1998; Brown et al., 2000), and soil (Baveye et al., 2002; Vogel et al., 2002). Authors of studies also comparing different materials generally reported individual REV for each specific material or sample (Baveye et al., 2002; Al-Raoush & Papadopoulos, 2010; Borges et al., 2018; Zhang et al., 2000).

In the present work, CT scanning was applied in the study of a 5 m long core of the Boda Claystone Formation (BCF) to get an accurate insight into the variability of the porosity and density of the rock-forming components. The main objective of this study was to calculate the representative elementary volume (REV) of porosity.

The basic REV concept introduced by Bear (1972) is shown in Fig. 1A. This idea says that if an infinitesimal cu-

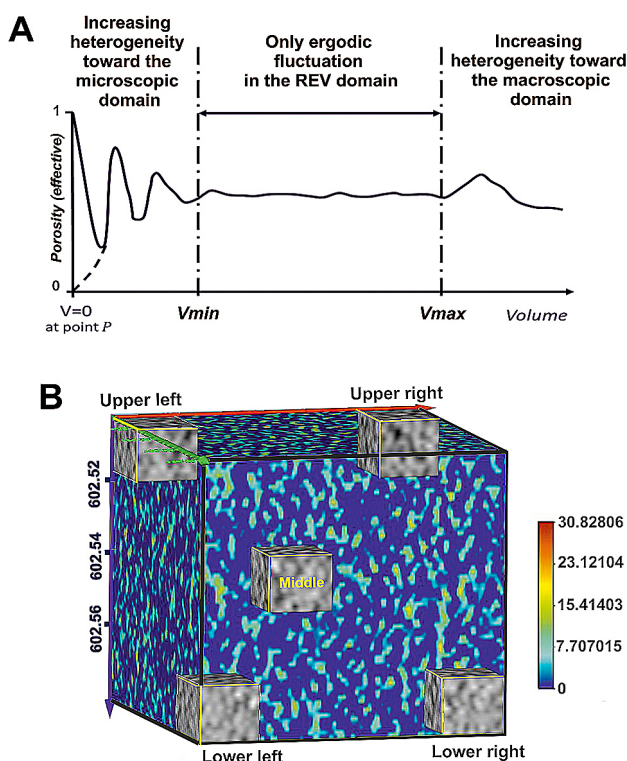


Fig. 1. A: Definition of the Representative Elementary Volume, REV (after Bear, 1972). B: locations of initial cubic volume.

bic elementary volume, at a point, is considered, its porosity can take two values, 0 or 1. If the point is inside a pore, the porosity at is 1, in the other case, the porosity is 0. When we increase the volume around gradually, the corresponding porosities alternate between 0 and 1. This region is labelled as the ‘Domain of microscopic’ (Fig. 1A, left-hand side). Beyond a particular volume around (Fig. 1A, V_{min}), these microscopic variations tend to decay, leaving only small-amplitude fluctuations that are due to the random distribution of pore sizes in the neighbourhood of (Fig. 1A, middle part). The homogenous region may become again heterogeneous after a particular volume (Fig. 1A, V_{max}). The region between V_{min} and V_{max} is called Representative Elementary Volume.

2. X-RAY COMPUTED TOMOGRAPHY (CT); QUANTITATIVE AND APPLIED

2.1. Quantitative data in CT scan images

X-ray computed tomography (CT) can provide unrivalled information about the internal structure of materials non-destructively from the meters down to the tens of nanometres length scales. It exploits the penetrating power of X-rays to obtain a series of two-dimensional (2D) radiographs of the object viewed from many different directions. This process is called a CT scan. A computed reconstruction algorithm is then used to create a stack of cross-sectional slices from these 2D projections (radiographs) of the object (Withers et al., 2021).

A single CT scan image is produced using a mono-energetic X-ray. As each X-ray beam passes through the sample, it attenuates varyingly, and the transmitted X-ray is received by a detector (Hounsfield, 1973). The attenuation is measured at many angles and reconstructed in a 3D matrix. The 3D distribution of the X-ray attenuation coefficient in reservoir rocks is dependent on variations in mineral composition (atomic number and density), porosity, and saturation. X-ray attenuation is physically determined mainly by photoelectric absorption and the Compton effect. Photoelectric absorption is dependent on the effective atomic number and is especially important at low energies (Yang et al., 2019; Withers et al., 2021). The Compton effect predominates at high energies and the associated X-ray attenuation is mainly controlled by density (Withers et al., 2021). Just as 2D images are made up of 2D pixels, 3D images are made up of many cubic volume elements called voxels (Withers et al., 2021). The X-ray attenuation can be determined using Beer Lambert’s law (Eq. 1). Each rotation of the X-ray source around the sample produces a cross-sectional image, which can then be stacked to form a 3D volume.

$$I = I_0 e^{-(\mu d)} \quad (1)$$

where I is the intensity of the transmitted X-ray, I_0 is the initial X-ray intensity, μ is the linear X-ray attenuation coefficient and d is the length of the X-ray path inside the object. When X-ray energy and intensity are kept constant, linear attenuation of X-ray occurs as a function of density, resulting in the sensitivity of CT images to density changes (Heismann et al., 2003; Duchesne et al., 2009).

Series of X-ray attenuation measurements are numerically processed (reconstructed) to show the spatial distribution of X-ray attenuation coefficients within the sample; the signal at each point in the reconstructed images referred to as CT numbers are expressed in Hounsfield units. The Hounsfield unit (HU) scale is a linear transformation of the original linear attenuation coefficient measurement into one in which the radiodensity of distilled water at standard pressure and temperature (STP) is defined as zero Hounsfield units (HU), while the radiodensity of air at STP is defined as – 1000 HU. The corresponding HU value is therefore given by:

$$HU = 10^3 \cdot \frac{\mu - \mu_w}{\mu_w} \quad (2)$$

where is the attenuation coefficient of the measured material, and is the attenuation coefficient of water. The X-ray attenuation coefficient is represented as CT numbers for a medical CT, which is calibrated to air with the value - 1000 and water with the value 0 according to the Hounsfield scale.

Grey-scale images are generally used to visualise the differences in X-ray attenuation. This process provides a digital 3D grey-scale representation (often referred to as a tomogram). This can be quantitatively analysed and virtually sliced in any direction or specific constituents can be digitally colour-coded to visualise the 3D morphology. For example, bright colours (high values) have low porosity and dark colours (low values) have high porosity in reservoir rocks with constant mineralogy and saturation (Földes et al., 2004; Wesolowski & Lev, 2005; Földes, 2011).

Measurements with X-ray CT are subject to a range of errors and image artifacts, including Beam hardening, star-shaped, positioning error, and machine error. Techniques used to minimise them were discussed in full by Van Geet et al. (2000), Ketcham & Carlson (2001), and Akin & Kovscek (2003).

2.2. Applied CT scan images

A core sample of BCF (Ib-4), about 5 m-long, was scanned at a high-resolution X-ray CT facility at the Institute of Diagnostic Imaging and Radiation Oncology, University of Kaposvar, Hungary. The CT measurements were performed on a Siemens Emotion 6 medical scanner. The instrument operates at 120 kVp (peak kilovoltage), with 250 mAs (milliampere-seconds) current, 1.0 s (sampling intervals). The lateral resolution was (0.1953 × 0.1953)

mm² with 1.25 mm of scan-slice thickness. The image reconstruction matrix was 512 × 512 pixels. The field of view (FOV) was approximately 9.99 cm. CT images are stored in a DICOM (Digital and Imaging Communications in Medicine) format. DICOM images are be easily read by 'classical' 3D volume rendering software (Abutaha et al., 2021^a).

Scans were made using a modified dual-scanning approach (Balázs et al., 2018). Usually, rock samples are dried in a vacuum oven at temperatures of 120 to 210 °F (50 to 100 °C). Drying is terminated when the samples reach a stable weight (Soeder, 1986). After six hours of vacuuming the sample, all pore water was removed, and CT measurements were acquired (scan of the dry core). The next phase was pumping water in the whole dried sample (saturation process). After an hour of relaxation, those slices that went under vacuumed then flooded condition were re-scanned. CT images were stored in a DICOM (Digital and Imaging Communications in Medicine) format. A DICOM file contains in its metadata the scanning parameters, i.e., Pixel Spacing and Slice Thickness attributes. These metadata are essential for geoscientific applications as they record the dimension (in millimeters) of each voxel in the x, y, and z direction.

The laboratory guaranteed that the DICOM files were free of any artifacts and that during the second scan, the same pixels were measured as during the first one. This image format is a standard in medical applications and can be easily read by 'classical' 3D volume rendering software (e.g., VOXLER).

For the present paper, we have calculated the porosity values for each voxel of the scanned slices from both scans (Moss et al., 1990; Abutaha et al., 2021 a).

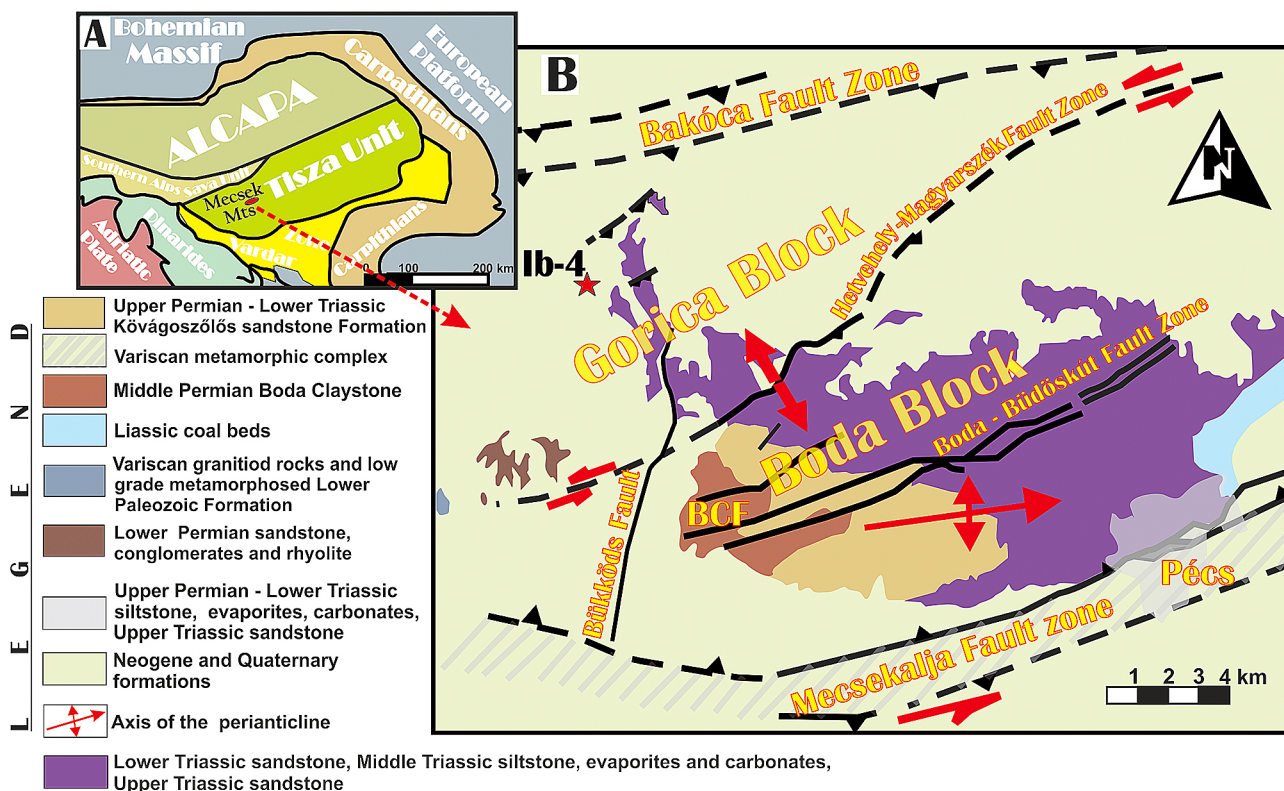


Fig. 2. A – Distribution of Boda Claystone Formation sequences in the Mecsek Hills area (after Haas & Péró, 2004); B – The studied core site, Ibafa 4 (Ib-4), marked by a red star in the upper left-hand corner.

3. GEOLOGICAL SETTING AND MINERALOGY

The Upper Permian sedimentary sequence of the Boda Claystone Formation (BCF) is where the studied sample has its place. It is located in the western Mecsek mountains, southern Transdanubia (southern Hungary) (Fig. 2A); it is known for 150 km². Ten percent of which can be found on the surface. This formation has been selected as a potential disposal repository rock formation for high-level nuclear waste (HLW) due to its low porosity, appropriate hydraulic conductivity, and absence of organic residues (Boisson, 2005). Two distribution areas of BCF are known (Fig. 2B), the western Mecsek mountains (a peri-anticlinal structure; ca. 700–900 m) and in the Gorica block (ca. 350 m). However, Gorica Block has only one borehole (Ib-4); it covered ca. 200 m of the complete sequence of BCF.

BCF was deposited in a shallow-water salt lake environment surrounded by dry to saline mudflats, under semi-arid to arid climatic conditions (Baraba's & Baraba's-Stuhl 1998; Máthé, 1998; Árkai et al., 2000; Varga et al., 2005; Máthé & Varga, 2012). The stratigraphical position, as well as the detailed geological information of the core sample studied, are shown in Fig. 3.

The main rock-forming minerals of BCF are clay minerals (10–55 wt %), albite (20–60 wt %), detrital quartz (5–30 wt %), carbonate minerals (calcite and dolomite; 10–50 wt %) and hematite (5–10 wt %) (Máthé, 1998, 2015; Árkai et al., 2000;

Varga et al., 2005, 2006). The illite–muscovite, and chlorite have also a remarkable occurrence; 15–50 wt % and 0–35 wt %, respectively. Otherwise, smectite, kaolinite, vermiculite, and mixed-layer clay minerals (illite/smectite, chlorite/smectite) are minors (Máthé, 1998, 2015; Árkai et al., 2000; Varga et al., 2005, 2006). The authigenic albite is present as albite cement (typical for all rock types of BCF), and few millimetre sized irregular vesicles filled with albite and carbonate minerals (typical for albitic claystone) In the Gorica block, same as the authigenic albite, the analcime is present as cement and pore-filling material. According to mineralogical investigations, amounts of analcime range between 8 and 25 wt % (Fedor et al., 2018).

According to the cooperation between the University of Szeged, GEOCHEM, and the Public Limited Company for Radioactive Waste Management (PURAM), the raw data sets of dry and flooded CT measurements of the core material were transferred to the University of Szeged for further analyses. Five larger blocks of the core material served as the basis of the present work. Only the texturally undamaged parts of the core blocks were analysed (Fig. 3).

4. METHODS

4.1. Pre-processing

Figure 4 shows the workflow followed to obtain the REV of voxel porosity. A 3D-nearest neighbour algorithm was used to build the 3D volumes of the scanned core blocks. This process resulted in two lattices, one for the vacuum dried and one for the saturated core volumes. The so-called scanning artifacts may obscure details of interest or cause the CT value of a single material to change in different parts of an image. The most commonly encountered artifact in CT scanning is beam hardening. Various methods have been developed to reduce or remove the effects of beam hardening (Van Geet et al., 2000; Ketcham & Carlson, 2001; Akin & Kovscek, 2003). One of these is subset the CT volumes. It means removing the 3D image's outer edges and only central volumes are handled in quantitative analysis.

For the identification of rock-forming components of the core sample, CT HU intervals defined by PURAM for characteristic rock types of BCF were used as follows: detrital fragments (coarse siltstone): < 2700 HU, fine siltstone: 2700–3150 HU, claystone: 3150–3300 HU, calcite and/or dolomite: 3300–3600 HU, and albite: > 3600 HU (Abutaha et al., 2021^a). The reality of the rock-forming components was compared with macroscopic core descriptions.

Calculation of the relative percentages of the rock-forming components for scanned core parts was a prerequisite of the definition of small-scale layers. These layers are called CT layers in the rest of this paper.

4.2. REV calculations

The REV is a function of the spatial position of point (Fig. 1A), where the volume-increasing process starts. Consequently; in the domain of REV, the porosity of such volume should not vary significantly across different parts of the sample (Fernandes et

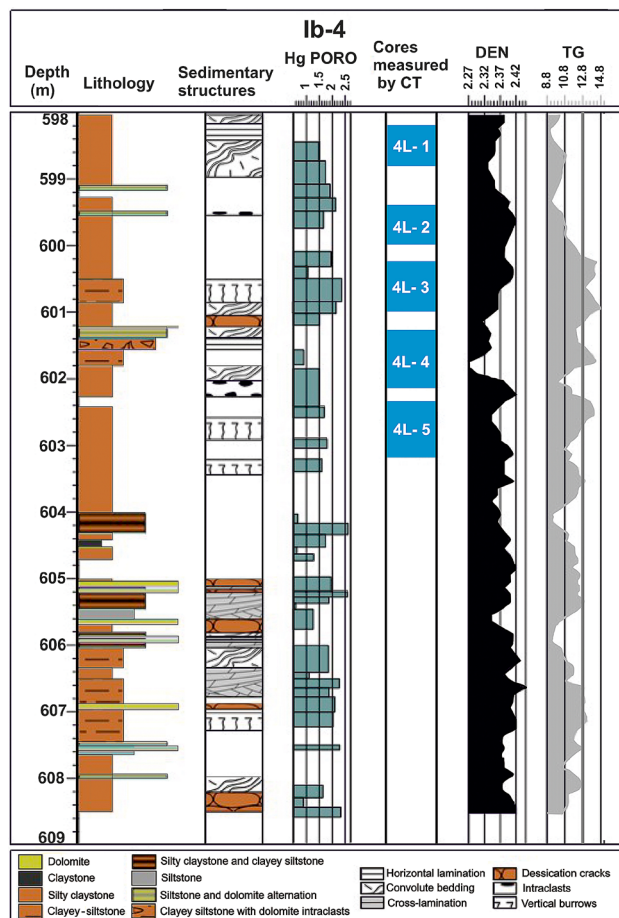


Fig. 3. The core and the intervals studied by CT. Abbreviations:

Hg Poro = Mercury Porosity, Den = Density log, TG = Natural Gamma log.

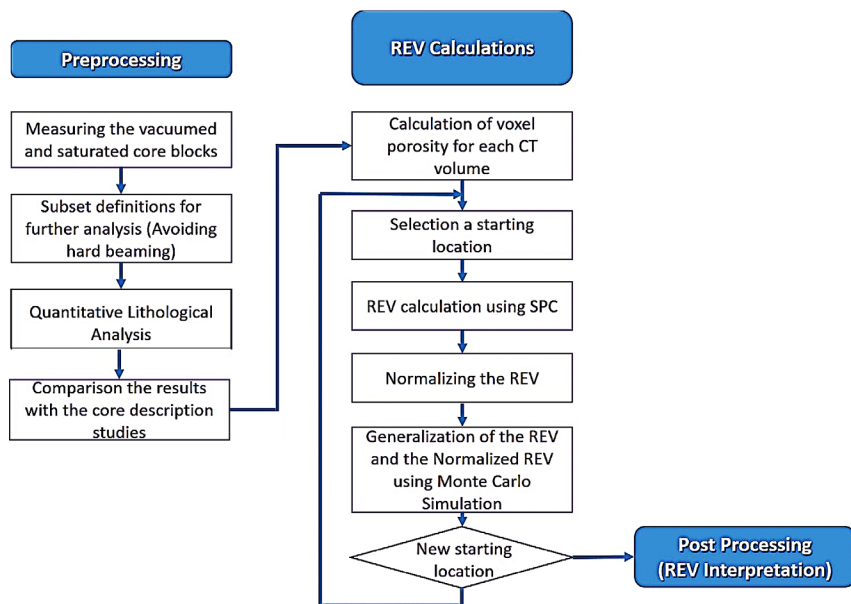


Fig. 4. The workflow.

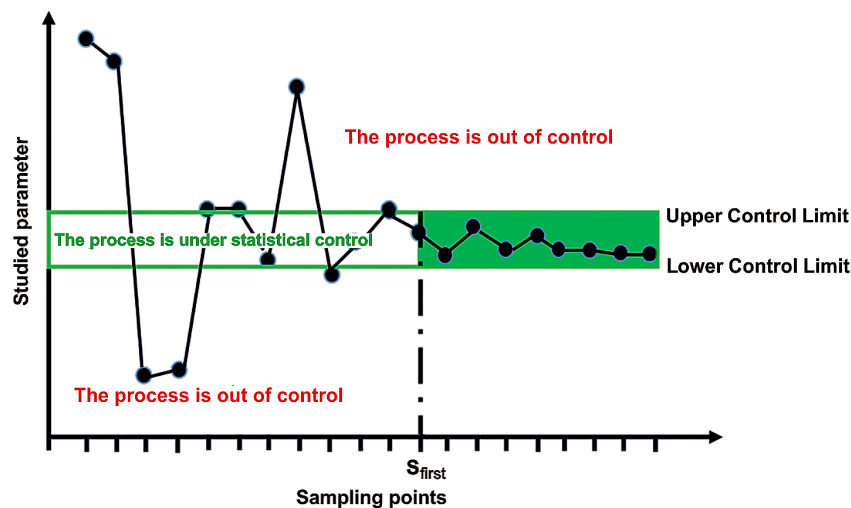


Fig. 5. The SPC chart

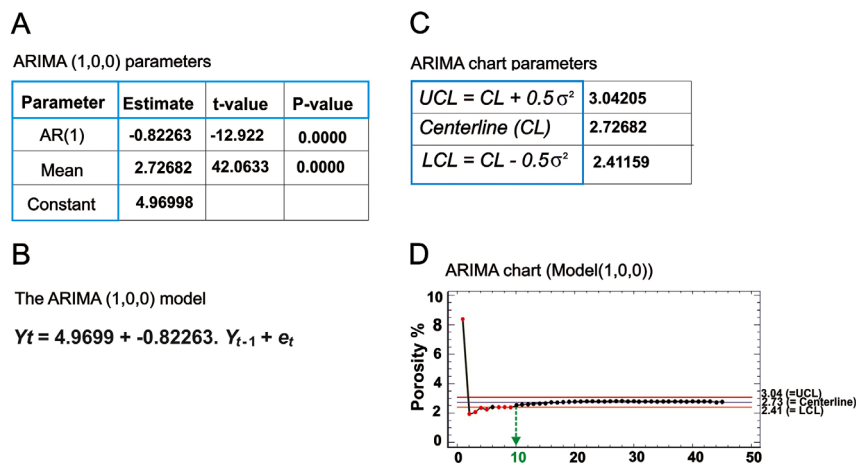


Fig. 6. An example of the applied ARIMA charts. A – Parameters of the selected model; B – The explicit form of the selected model; C – Parameters of the ARIMA chart; D – ARIMA chart with the indication of the volume step where the REV can be defined.

al., 2012). In this work, we pointed out five different starting positions, within the studied CT volumes to calculate REV (Fig. 1B).

The calculations were started with a traditional point-centred cube geometry, in which dimensions were increased symmetrically in all directions from a single-voxel starting point. The averages of the acquired porosity values were then plotted on a chart of Statistical Process Control (SPC). Control limits are the standard deviations located above (UCL) and below (LCL) the centreline of an SPC chart. If the voxel porosity measurements are within the control limits (tolerance margins), it indicates that the process is in control (Fig. 5); non-random pattern in the distribution. If there are data points outside the tolerance margins, it indicates that a process is out of control (Montgomery, 1997; Russo et al., 2012; Geiger, 2018; Abutaha et al 2021^b).

The term ‘non-random pattern’ can be matched with the REV domain since both express ‘controlled’ processes (Figs. 1A,5). In Fig. 5 the studied parameter has only controlled values at the sampling point beyond S_{first} . This sample point corresponds with the minimum volume from which the REV can be defined (Figs. 1A,5). That is, the minimum volume of REV can be identified by using SPC.

In general, the practice of SPC analysis consisted of three steps: understanding the process and specification limits, eliminating special sources of variations, and monitoring the ongoing process (Polhemus, 2005). In the present study, the last step is not used. Normally, SPC works under the assumption that the data observed are independent. However, in our case, a continuous transition violating independence between the different rock-forming components must be assumed. ARIMA (Auto-Regressive Integrated Moving Average) charts are designed to handle such situations (e.g., Box et al., 1994; Polhemus, 2005; Russo et al., 2012).

Figure 5 illustrates a typical example of the applied analysis with ARIMA charts for the first CT volume. The starting point was at the upper left side of the volume. In Fig. 6A, the components of the fitted ARIMA (1,0,0) model are shown. The explicit form of this model is a linear combination of a constant, one

autoregressive term, and an error term (Fig. 6B). The calculated centreline (average) and the UCL and LCL lines are shown in Fig. 6C. Finally, in Fig. 6D, the ARIMA chart can be seen, where the red dots indicate those parts of the series where severe deviations can be detected from the ARIMA (1,0,0) model. From the 10th incremental step, a series of averaged porosity values are within the UCL and LCL. That is, the porosity is fully controlled. Consequently, the minimum volume of REV can be identified as the volume belonging to the 10th incremental step (64.75 cm³).

Such calculations were performed for each of the 20 CT volumes (Tab. 1). A particular REV value obtained may also depend on the size of the corresponding CT volume, which makes the comparison complicated. To circumvent this problem, the REV values were normalised by the studied CT volumes (Tab. 1). In this way, REV could be expressed as the percentage of the studied volume.

The Monte Carlo simulation focuses on constantly repeating random samples to achieve certain results. Once the simulation is complete, the results are averaged to provide an estimate. We applied this approach to simulate 1 000 outcomes of REV calculated for each CT volume. By doing so, we assumed that those parts of the core studied fairly and representatively described the composition of the rock types of the entire core (Tab. 2).

The prior procedure was five times iterated by varying the location of starting voxel volume; upper left, upper right, lower left, lower right, and middle. Table 3 shows the mean REV – porosities of CT volumes.

4.3. Post-processing

When investigating the REV, it is essential to fully understand spatial distribution and variability of petrophysical properties of the core sample studied. Abutaha et al. (2021^a) used a Boolean function to show the 3D spatial distributions of voxel-porosity by rock types. In that way, a straight connection between the rock-forming components and the voxel porosities would derive. In the present work, the Boolean lattices were built up for 4L-1 and 4L-2 core volumes to visualise the three-dimensional distribution of voxel-porosities of rock-forming components. In addition, relying on Abutaha et al. (2021^b), layers boundaries of the 4L-1 and 4L-2 core volumes were defined. The layer-averaged voxel-porosity frequencies were calculated in each layer to quantify the variability of pores distributions across different rock components.

Linear correlation coefficients were calculated between any two pairs of rock-forming components and corresponding average porosities over the CT layers. Only those correlations were regarded as important relations, where the 25 % ($r^2 = |0.5|$) of the variance of a variable was predictable from the other one.

5. RESULTS AND INTERPRETATIONS

5.1. Actual and simulated REV values

Detailed calculations of the REV (cm³) and the normalised REV (%) of the twenty CT volumes of each location are summarised in

Tab. 1. Summary table of REV calculations.

Block No.	CT Volume No.	Voxel Volume of the CT brick (cm ³)	REV (cm ³)					Normalised REV (%) (REV (cm ³) / CT brick volume) * 100 %				
			Upper left	Upper right	Lower left	Lower right	Middle	Upper left	Upper right	Lower left	Lower right	Middle
1L1	volume 1	222.00	64.75	16.90	4.58	159.68	47.50	29.17	7.61	2.06	71.93	21.40
	volume 2	236.00	74.08	10.62	36.85	26.57	24.00	31.39	4.50	15.61	11.26	10.17
	volume 3	42.53	19.12	16.33	1.82	2.73	0.45	44.96	38.41	4.28	6.42	1.06
	volume 4	85.05	19.05	13.23	10.56	17.72	31.19	22.40	15.55	12.41	20.83	36.67
	volume 5	70.88	58.73	8.10	0.32	16.64	9.90	82.86	11.43	0.45	23.48	13.97
1L2	volume 6	96.26	35.77	1.31	31.13	2.27	6.25	37.16	1.36	32.34	2.36	6.49
	volume 7	313.88	95.33	16.90	13.94	17.90	1.97	30.37	5.38	4.44	5.70	0.63
	volume 8	265.05	41.53	0.38	87.12	3.87	0.85	15.67	0.14	32.87	1.46	0.32
2L1	volume 9	101.84	41.53	10.62	2.08	0.42	1.35	40.78	10.43	2.04	0.41	1.33
	volume 10	439.92	64.75	41.97	55.12	9.24	0.12	14.72	9.54	12.53	2.10	0.03
	volume 11	205.92	56.24	16.66	21.37	31.43	0.81	27.31	8.09	10.38	15.26	0.39
	volume 12	198.43	41.53	1.26	13.09	16.65	0.81	20.93	0.64	6.60	8.39	0.41
4L1	volume 13	126.00	7.87	1.30	50.50	51.52	0.12	6.25	1.03	40.08	40.88	0.09
	volume 14	277.20	41.53	13.52	41.51	44.70	101.60	14.98	4.88	14.97	16.12	36.65
	volume 15	136.42	20.26	8.17	10.25	26.90	3.62	14.85	5.99	7.51	19.72	2.65
	volume 16	26.87	16.89	0.38	14.55	2.01	5.39	62.85	1.41	54.13	7.48	20.06
	volume 17	74.40	36.83	8.17	40.99	1.49	0.12	49.50	10.97	55.10	2.00	0.16
4L2	volume 18	92.16	7.87	0.16	2.96	6.50	6.25	8.54	0.17	3.21	7.06	6.78
	volume 19	105.12	32.25	0.38	6.75	8.47	7.87	30.68	0.36	6.42	8.05	7.49
	volume 20	442.08	149.30	144.88	15.68	22.24	107.94	33.77	32.77	3.55	5.03	24.42

Tab. 1. As of now, the term of location is used to show the position of the initial volume of the REV calculation.

Table 2 shows, that the average REV values range from 16.56 up to 46.26 cm³. The largest REV value corresponds to the upper left location, while the smallest REV relates to the upper right location (Tab. 2).

The normalised REV, in the upper right and the middle locations, give almost equal volume percentages; ≈ 9 %. They also have almost similar values at the lower right and lower left locations: 14 % and 16 % (at the scale of the studied core volume). However, the upper left location displays an extremely high average REV percentage; it is about 31 % (Tab. 2).

The Monte Carlo simulation with 1 000 runs was used to simulate the long-run properties of REV and the normalized REV of voxel-porosity. The results are seen in Tab. 2 (the last two columns). In the studied core volume, the average range of the simulated REV extends from 54 to 65 cm³. Notwithstanding, the middle location of REV shows a much smaller value around 42 cm³.

According to the simulation of the normalised REV values,

Tab. 2. Summary statistics of actual and simulated REV values.

Starting point	Statistics characters	REV (cm ³)	Normalized REV (%)	Simulated REV at 1000 runs (cm ³)	Simulation of normalized REV at 1000 runs (%)
Upper left	Avg (cm ³)	46.26	30.96	64.80	39.65
	Md (cm ³)	41.53	29.77	60.53	37.98
	STD	33.39	18.79	30.56	15.47
	Min (cm ³)	7.87	6.25	7.45	8.70
	Max (cm ³)	149.30	82.26	149.75	78.19
Upper right	Avg (cm ³)	16.56	8.53	53.77	15.71
	Md (cm ³)	9.39	5.69	49.24	14.67
	STD	31.76	10.32	32.47	8.32
	Min (cm ³)	0.16	0.14	0.51	0.73
	Max (cm ³)	144.88	38.41	143.55	36.64
Lower right	Avg (cm ³)	23.45	13.80	61.44	41.34
	Md (cm ³)	16.45	7.77	55.68	40.11
	STD	35.16	16.84	34.96	17.96
	Min (cm ³)	0.42	0.41	1.44	2.83
	Max (cm ³)	159.83	71.93	158.02	87.31
Lower left	Avg (cm ³)	33.35	16.05	55.59	23.86
	Md (cm ³)	28.06	8.95	51.75	22.19
	STD	30.44	17.23	27.60	11.00
	Min (cm ³)	2.08	0.45	2.53	1.96
	Max (cm ³)	131.42	55.10	130.85	53.94
Middle	Avg (cm ³)	17.91	8.56	42.23	15.53
	Md (cm ³)	4.50	4.57	38.11	14.73
	STD	32.16	12.16	23.56	7.98
	Min (cm ³)	0.12	0.03	0.37	0.13
	Max (cm ³)	107.94	36.67	107.04	35.61

Tab. 3. Summary statistics of the mean porosities of the REV.

	REVs porosity averages (%)				
	Upper left	Upper right	Lower right	Lower left	Middle
Average	2.52	2.58	2.55	2.47	2.78
Median	2.52	2.62	2.54	2.51	2.81
Standard deviation	0.21	0.22	0.22	0.185	0.26
Minimum	2.08	2.09	2.01	2.10	2.23
Maximum	2.88	2.92	2.88	2.85	3.05

the percentages at the scale of the studied core volume (from highest to smallest) are as follows: upper left location 40 %, the lower right location 41.34 %, and the lower-left location 23.86 %, respectively. The upper right and the middle locations have almost the same percentage volumes around 15.5 %.

The average effective voxel porosity of BCF is approximately 2.55 %. In Tab. 3, the REV porosities calculated from the sample's corners (upper left, upper right, lower left, and lower right) have mostly coincided with the general BCF average voxel porosities of 2.46 – 2.58 %. However, the middle location has an exceptional larger REV porosity value (~ 2.8 %).

The REV porosity of the middle position showed an odd high value (~ 2.8 %). To understand this remarkable result, further quantifying analyses of porosity distribution were applied to the 2 m bottom of the studied core sample (4L-1 and 4L-2 core volumes).

Quantitative analysis of porosity in 4L-1 and 4L-2 volumes

In Fig. 7, each 3D brick of the dry scan includes five-rock constituents: detrital fragments, fine siltstone, claystone, carbonate, and albite. The voxel porosity averages of these rock-forming components were calculated using dual CT scanning (Abutaha et al., 2021^a).

Figure 7 shows the voxel porosities of the analysed CT volumes (second column). From the third to seventh columns, the porosity characters of the five rock-forming components are detailed. In the eighth column of Fig. 7, the porosities of the detrital fragments and the albite nests are pooled. The ninth column shows the small-scale layers defined by the dominant rock-forming component (Abutaha et al., 2021^b). Finally, the last column is for their average porosity.

Based on Fig. 7, the following facts could be derived: 1) The spatial distribution of the porosities of the detrital fragments and the albite nests are very similar (Fig. 7, the third and the seventh columns); 2) The higher the amount of the detrital fragments and albite, the larger the CT-layer-averaged porosity (Fig. 6, the eighth and the tenth column); 3) The alternation of the CT layers with high and low layer-averaged porosity shows a cyclical pattern (Fig. 6, the tenth column).

In a former study, the CT-layers were classified into three genetic groups based on data-mining techniques, by which the K-fold cross-validation algorithm was used to determine the cluster distribution number of the calculated voxel porosities (Abutaha et al., 2021^a). The first group was CT-layer with dominantly matrix porosity, where 75 % of the voxel porosities were smaller than 7 %. The second group was called CT-layers with dominantly macro-porosity. In this group, 75 % of the voxel porosity ratios

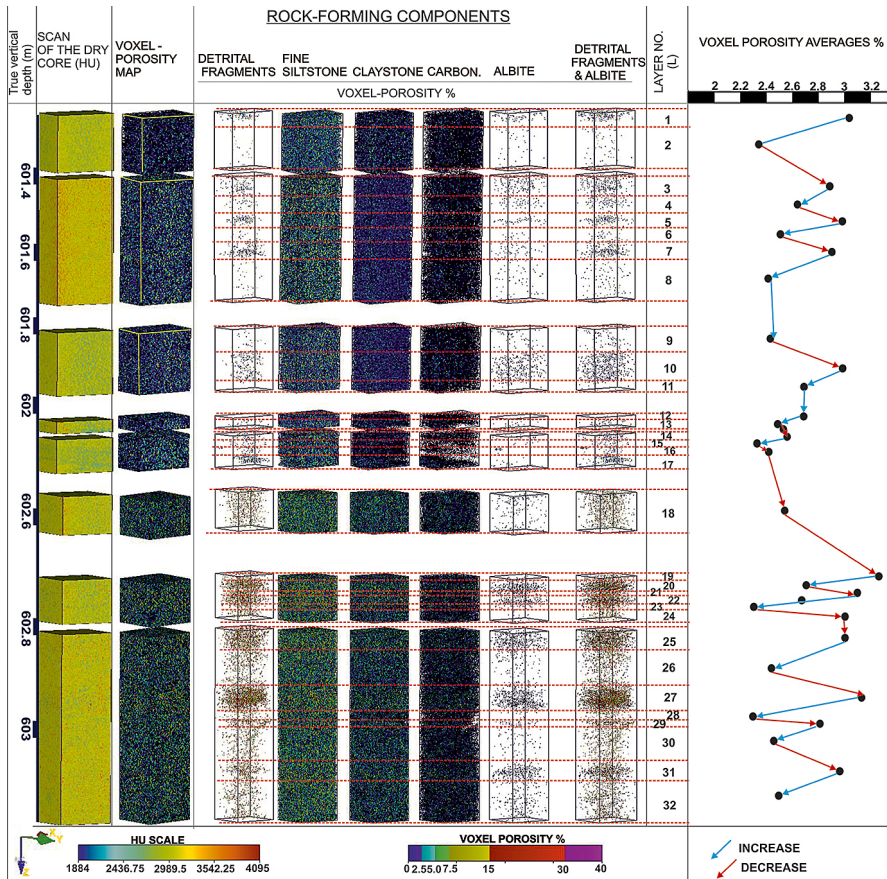


Fig. 7. Average porosity values of the five rock-forming components; boundaries of layers, and voxel-porosity averages of each layer were also defined.

were larger than 7 % and smaller than 19 %. The larger than 19 % voxel porosities were regarded as outliers and extremities. Finally, the third group was for no-porosity (pores ~ 0).

Table 4 shows two groups of small-scale layers. The first group (Tab. 4A) summarises the relative frequencies of the tabulated

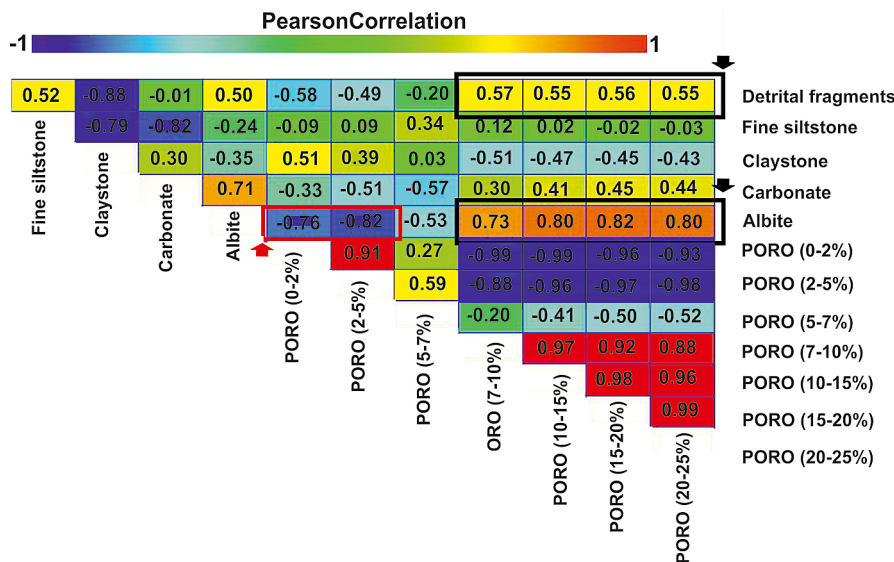


Fig. 8. The linear (Pearson) correlation coefficients for averaged porosity cut-off ratios and rock-forming components.

layer-averaged porosity values for layers containing a significant amount of detrital fragments and albite nests. Part B of Tab. 4 includes the same tabulation for layers that do not have a considerable amount of detrital fragments and albite nests. The cumulative percentages of the micro and matrix porosities are calculated (Tab. 4).

The cumulative percentages of the macro and matrix porosities are significantly different in the two groups. They suggest that the presence of both the detrital fragments and the albite constituents might increase the average porosity by enhancing the presence of the macro porosity. Conversely, the absence of detrital fragments and albite might intensify the matrix porosity. Matrix pores can be related to the presence of dense proportions of claystone-siltstone components (e.g., Ahmad et al., 2018).

The linear correlation coefficients were calculated between the weight percentages of the rock-forming components and corresponding average porosities (Fig. 8). Figure 8 shows that the detrital fragments component has a moderate relationship with the 7 – 25 % interval of the macro porosity; the r-value is around 0.55 (Fig. 8, upper black arrow). Whereas the albite has a significantly stronger linear relation to the macro pores; the corresponding r-value is around 0.8 (Fig. 8, lower black arrow). The pore spaces (macro pores) might be created within the detrital fragments because of the larger relative grain size.

The correlation structure of Fig. 8 can prove this theory. The high correlation coefficients belonging to the weight percentage of albite show, that albite plays a substantial role in the generation of macro porosity. The negative correlation coefficient between the weight percentage of albite and the frequency of very small voxel porosities (Fig. 8, red arrow) can be explained by the process of CT measurement. During the saturation phase, the difference between the pore pressure and the injected water pressure may force some movable small particles to get out from some semi-filled pore space. In this way, the pore volume increases in the exhausted pores (Simon & Anderson 1990; Zhou et al., 1995;

Tab. 4. Tabulated relative frequencies of the average voxel porosities by layers.

Layers	Matrix porosity	Macro-porosity	Extrem large values
	(0 – 7)%	(7 – 19)%	(20 – 25)%
A			
L1	82.08	17.87	0.44
L3	83.35	16.62	0.29
L5	82.40	17.56	0.37
L7	83.26	16.70	0.30
L10	82.81	17.16	0.36
L20	81.22	18.69	0.55
L22	82.38	17.58	0.39
L25	82.73	17.24	0.33
L27	81.65	18.28	0.52
L29	84.15	15.79	0.19
L31	83.37	16.60	0.30
Average	82.68	17.28	0.37
B			
L2	87.96	12.00	0.05
L4	85.80	14.03	0.15
L6	86.38	13.50	0.12
L8	87.27	12.65	0.07
L9	87.21	12.70	0.08
L11	88.56	11.40	0.04
L12	88.61	11.30	0.03
L13	80.92	12.98	0.09
L14	84.49	13.46	0.06
L15	86.66	13.26	0.07
L16	87.75	12.20	0.05
L17	88.06	11.88	0.05
L18	87.44	12.49	0.07
L19	85.84	14.04	0.12
L21	85.20	14.49	0.28
L23	85.26	14.56	0.17
L24	88.39	11.56	0.04
L26	87.33	12.60	0.07
L28	85.50	14.34	0.15
L30	87.59	12.36	0.05
L32	87.04	12.90	0.06
Average	87.02	12.89	0.09

Hayatdavoudi & Ghalambor 1996; Al-Yaseri et al., 2015). In our case, releasing albite particles from pore volume could generate an additive macro pore space resulting from particles' migration. Those additive macro pores might cause a higher macro porosity measurement, resulting in a higher overall porosity ratio of each CT layer (Fig. 7, last column). However, if these small particles (i.e., albite) meet a narrow pore throat during their movement, they could cause throats plugged, by which the corresponding pore volume would decrease (Ahmad et al., 2018). This process results in an erroneous negative correlation coefficient between the voxel porosity and the albite content (cf. Fig. 9).

Figure 9 gives additional visual clues as to the presence of albite could be partly responsible for raising macro porosity according to removing (migrating) the albite cement from pore

volume (Fig. 9, red arrows), as well as reducing porosity by filled pores (Fig. 9, white arrows).

5.2. REV interpretation

The frequent appearance of detrital fragments and albite intercalations reflects a repetitive pattern of porosity distributions in the middle part of the studied succession (Fig. 7). As the initial voxel volume started in such a medium (where albite and detrital fragments took place), the average porosity variations of the continuous volume transitions would become minimal at a high REV porosity value (~ 2.8 %) because the intensive macro pores exist. However, the scene was different when the initial voxel volume started from any four sample's corners (upper left, upper right, lower left, and lower right). The sample's core (centre) was

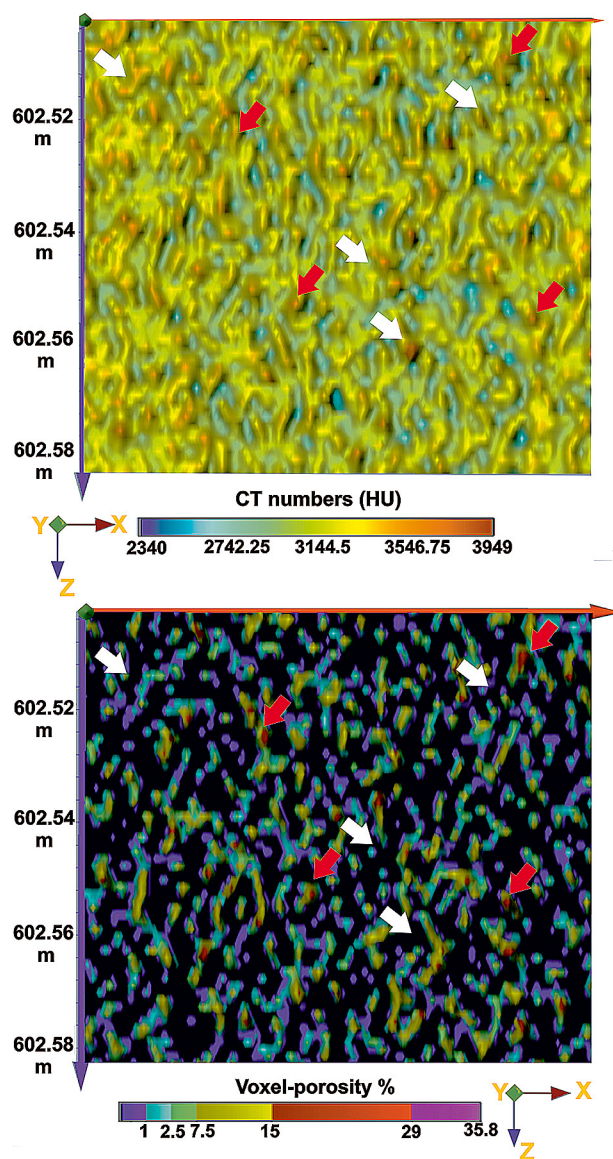


Fig. 9. Albite nests. On the left, the albite voxels appear with very high CT numbers. The corresponding voxel porosities are shown for the same slice on the right. The red arrows indicate albite removed from pore volumes, and white arrows point to the albite-filled pores

surrounded by a dense proportion of claystone-siltstone (mostly lacking albite and detrital fragments); matrix-porosity is highly expected (Fig. 7 – 8th column). Therefore, since the continuous transition of the initial voxel volume occurred within the matrix porosity medium, the REV porosity value was significantly lower than that obtained from the middle. It was pretty close to the voxel porosity average of BCF (~ 2.5 %). That is, the REV porosity value relies on the spatial position of the volume increasing process starts (initial volume).

6. SUMMARY AND CONCLUSION

3D X-ray computed tomography images enabled obtaining accurate quantification of the variability of the porosity and the density of the rock-forming components. Such quantification allowed performing the REV analysis of porosity variations. CT scanning is applied in a 5m core sample of the Boda claystone formation (BCF) in the current work. This study's main objective is to calculate REV of porosity. The REV calculation was carried out five times using the ARIMA SPC technique across the core sample. Each time it would start from a different cubic volume position. The obtained REV values were generalised using the Monte-Carlo simulation method, and the variations of REV porosity averages were thoroughly studied.

The general average range of REV values was from 16.56 to 46.26 cm³. The Monte Carlo simulation with 1 000 runs was used to simulate the long-run properties of REV and the normalised REV of voxel porosity. The simulated REV range was 42–65 cm³. Their volume percentages were 15.5 % and 40 %, respectively. The REV porosity averages calculated from any sample's corners (upper left, upper right, lower left, and lower right) were exhibited coincident approximations with the general BCF average voxel porosity; 2.47–2.58 %. However, the middle site gave the oddity value, which was much higher than the rest of the REV porosity averages; it was around 2.8 %.

The remarkable result associated with the highest REV porosity was studied deeply by further quantitative porosity analyses application. Accordingly, the following conclusions were derived: 1) Both detrital fragments and albite constituents might influence the averaged porosity proportions of the studied layers by enhancing the presence of macro-porosity ratios (7–25 %). Conversely, the absence of detrital fragments and albite might intensify the matrix porosity ratios (0–7 %). Matrix (throat) pores are almost related to dense proportions of claystone-siltstone components; 2) Although the detrital fragments might be a factor in the macro pores presence, the albite almost plays a significant part in developing macro porosity; 3) The saturation process of the core sample studied was the key to interpreting the dual-role of the albite. Hence, the albite particles could release and re-deposited downstream in pore throats during the core sample saturation process. Compiling its particles might be causing throats plugged (decreasing porosity). Otherwise, releasing albite particles from pore volume might generate an extra macro pore space (increasing porosity ratio).

As a result, when the initial voxels started from a medium where the macro porosity is expected to exist primarily (detrital

fragments and albite took place), the higher REV porosity was gained (~ 2.8 %). Alternatively, when the volume of the initial voxel occurred within the matrix porosity medium (barely presence of albite and detrital fragments), the REV porosity ratio would be < 2.8 %. That is to say, the middle part of the studied sample might not be adequate to be considered as an initial voxel volume of the REV calculation because its REV porosity value was significantly higher (~ 2.8 %) than the average of the effective voxel porosity of BCF (~ 2.5 %).

References

- Abutaha S.M., Geiger J., Gulyás S. & Fedor F., 2021^a: Evaluation of 3D small-scale lithological heterogeneities and pore distribution of the Boda Claystone Formation using X-ray computed tomography images (CT). *Geologia Croatica*, 74, 3, 305–318. doi: 10.4154/gc.2021.17.
- Abutaha S.M., Geiger J., Gulyás S. & Fedor F., 2021^b: Assessing the representative elementary volume of rock types by X-ray computed tomography (CT) – a simple approach to demonstrate the heterogeneity of the Boda Claystone Formation in Hungary. *Geologos*, 27, 3, 157–152. doi: 10.2478/logos-2021-0018
- Ahmad K.M., Kristály F. & Turzo Z., 2018: Effects of clay mineral and physico-chemical variables on sandstone rock permeability. *Journal of Oil, Gas and Petrochemical Sciences*, 18–26. doi:10.30881/jogps.00006
- Akin S. & Kovscek A.R., 2003: Computed tomography in petroleum engineering research. In: Mees F., Swennen R., Van Geet M. & Jacobs P. (Eds): Application of X-ray computed tomography in the geosciences. *Special Publication, Geological Society of London*, 215, 23–38.
- Al-Raoush R. & Willson C.S., 2005: Extraction of physically-representative pore network from unconsolidated porous media systems using synchrotron microtomography. *Journal of Hydrology* 23, 274–299.
- Al-Raoush R. & Papadopoulos A., 2010: Representative elementary volume analysis of porous media using X-ray computed tomography. *Powder Technology*. 200, 1–2, 69–77.
- Al-Yaseri A.Z., Lebedev M., Vogt S.J., Johns M.L., Barifcani A. & Iglauer S., 2015: Pore-scale analysis of formation damage in Bentheimer sandstone with in-situ NMR and micro-computed tomography experiments. *J. Petrol. Sci.*, 129, 48–57. doi: 10.1016/j.petrol.2015.01.018.
- Árkai P., Balogh K., Demény A., Fórizs I., Nagy G. & Máthé Z., 2000: Composition, diagenetic and post-diagenetic alterations of a possible radioactive waste repository site: The Boda Albitic Claystone Formation, southern Hungary. *Acta Geologica Hungarica*, 43, 351–378.
- Balázs G.Y.L., Lublőy É. & Földes T., 2018: Evaluation of concrete elements with X-Ray computed tomography. *Journal of Materials in Civil Engineering*, 30, 1–9.
- Barabás A. & Barabás-Stuhl Á., 1998: Stratigraphy of the Permian formations in the Mecsek Mountains and its surroundings. In: Stratigraphy of geological formations of Hungary. Geological and Geophysical Institute of Hungary, 187–215 p. (in Hungarian)
- Baveye P., Rogasik H., Wendroth O., Onasch I. & Crawford J.W., 2002: Effects of sampling volume on the measurement of soil physical properties: simulation with X-ray tomography data. *Measurement Science and Technology*, 13, 775–784.
- Bachmat Y. & Bear J., 1987: On the concept and size of a representative elementary volume (Rev). In: Bear J. & Corapcioglu M.Y. (Eds.): Advances in Transport Phenomena in Porous Media, *NATO ASI Series*, 128, 3–20.

- Bear J. & Bachmat Y., 1990: Introduction to Modeling of Transport Phenomena in Porous Media. Kluwer Academic Press, Dordrecht, 575 p.
- Bear J., 1972: Dynamics of fluids in porous media. Dover Publications Inc., New York, 764 p.
- Biswal B., Manwart C. & Hilfer R., 1998: Three-dimensional local porosity analysis of porous media. *Physica A: Statistical Mechanics and its Applications*, 255, 3–4, 221–241.
- Boisson J.Y., 2005: Clay Club catalogue of characteristics of argillaceous rocks, Radioactive waste management, OECD Nuclear Energy Agency, 72 p. ISBN 92-64-01067-X
- Borges J.A.R., Pires L.F., Cassaro F.A.M., Roque W.L., Heck R.J., Rosa J.A. & Wolf F.G., 2018: X-ray microtomography analysis of representative elementary volume (REV) of soil morphological and geometrical properties. *Soil Tillage Research*, 182, 112–22.
- Box G.E.P., Jenkins G.M. & Reinsel G.C., 1994: Time series analysis: Forecasting and control. 3rd Edition. Prentice Hall, Englewood Cliff, New Jersey, 619 p.
- Brown G.O., Hsieh H.T. & Lucero D.A., 2000: Evaluation of laboratory dolomite core sample size using representative elementary volume concepts. *Water Resources Research*, 36, 1199–1208.
- Chang C.S. & Gao J., 1995: Second-gradient constitutive theory for granular material with random packing structure. *International Journal of Solids and Structures*, 32, 2279–2293.
- Clausnitzer, V. & Hopmans J.W., 1999: Determination of phase-volume fractions from tomographic measurements in two-phase systems. *Advances in Water Resources*, 22, 577–584.
- Duchesne M.J., Moore F., Long B.F. & Labrie J., 2009: A rapid method for converting medical Computed Tomography scanner topogram attenuation scale to Hounsfield Unit scale and to obtain relative density values. *Engineering Geology*, 103, 100–105.
- Fedor F., Máthé Z., Ács P. & Koroncz P., 2018: New results of Boda Claystone research - genesis, mineralogy, geochemistry, petrophysics. In: Norris S., Neeft E.A.C. & Van Geet M. (Eds.): Multiple Roles of Clays in Radioactive Waste Confinement. *Geological Society, London, Special Publications*, 482 p., doi: 10.1144/SP482.13
- Feyel F. & Chaboche J.-L., 2000: FE2 multiscale approach for modelling the elasto-viscoplastic behavior of long fiber SiC/Ti composite materials. *Computer Methods in Applied Mechanics and Engineering*, 183, 309–330.
- Földes T., 2011: Integrated processing based on CT measurement. *Journal of Geometry and Physics*, 1, 23–41.
- Földes T., Kiss B., Árgyelán G., Bogner P., Repa I. & Hips K., 2004: Application of medical computer tomography measurements in 3D reservoir characterization. *Acta Geologica Hungarica*, 47, 63–73.
- Fernandes J., Appolonib C. & Fernandesc C., 2012: Determination of the Representative Elementary Volume for the Study of Sandstones and Siltsstones by X-Ray microtomography. *Materials Research*, 15, 4, 662–670. doi: 10.1590/S1516-14392012005000081.
- Fitch P, Lovell M., Davies S., Pritchard T. & Harvey P., 2015: An integrated and quantitative approach to petrophysical heterogeneity. *Marine and Petroleum Geology*, 63, 82–96.
- Frazer G., Wulder M. & Niemann K., 2005: Simulation and quantification of the fine scale spatial pattern and heterogeneity of forest canopy structure: a lacunarity based method designed for analysis of continuous canopy heights. *Forest Ecology and Management*, 214, 65–90.
- Geiger J., 2018: Statistical process control in the evaluation of geostatistical simulations. *Central European Geology*, 6, 1, 50–72.
- Hayatdavoudi A. & Ghalambor A., 1996: Controlling formation damage caused by kaolinite clay minerals: Part I. In: SPE Formation Damage Control Symposium, *Society of Petroleum Engineers*, SPE-31118-MS. doi: 10.2118/31118-MS.
- Heismann B.J., Leppert J. & Stierstorfer K., 2003: Density and atomic number measurements with spectral x-ray attenuation method. *Journal of Applied Physics*, 94, 2073–2079.
- Hounsfield G.N., 1973: Computerized transverse axial scanning (tomography). 1. Description of system. *British Journal of Radiology*, 46, 1016 – 1022.
- Ketcham R.A. & Carlson W.D., 2001: Acquisition, optimization and interpretation of X-ray computed tomographic imagery: applications to geosciences. *Computational Geosciences*, 27, 381–400.
- Konrád G.Y., Sebe K., Halász A. & Babinszki E., 2010: Sedimentology of a Permian playa lake: The Boda Claystone Formation, Hungary. *Geologos* 16, 27–41.
- Kouznetsova V., Brekelmans W.A.M. & Baaijens F.P.T., 2001: An approach to micro–macro modelling of heterogeneous materials. *Computational Mechanics*, 27, 37–48.
- Kouznetsova V., Geers M.G.D. & Brekelmans W.A.M., 2002: Multi-scale constitutive modelling of heterogeneous materials with a gradient-enhanced computational scheme. *International Journal for Numerical Methods in Engineering*, 54, 1235–1260.
- Máthé Z. & Varga A., 2012: “Ízesítő” a permi Bodai Agyagko Formáció öskörnyezeti rekonstrukciójához: kosó utáni pseudomorfózák a BAT-4 fúrás agyagkomintáiban. [“Seasoning” of the palaeoenvironmental reconstruction of the Permian Boda Claystone Formation: pseudomorphs after halite in the claystone samples of the deep drillings BAT-4]. *Földtani Közlöny*, 142, 201–204 [in Hungarian with English summary].
- Máthé Z., 1998: Summary report of the site characterization program of the Boda Siltstone Formation. *Mecsek Ore Environment Company*, Pécs, 4.
- Máthé Z., 2015: Results of mineralogical, petrological and geochemical investigation of Boda Claystone Formation. PhD thesis summary, ELTE Department of Petrology and Geology, Budapest, 1-6p. [in Hungarian]
- Montgomery D.C., 1997: Introduction to Statistical Quality Control. John Wiley and Sons, New York, 759 p.
- Moss R.M., Pepin G.P. & Davis L.A. 1990: Direct measurement of the constituent porosities in a dual porosity matrix. SCA conference, 9003
- Muhlhaus H.B. & Oka F., 1996: Dispersion and wave propagation in discrete and continuous models for granular materials. *International Journal of Solids and Structures*, 33, 271–283.
- Peerlings R.H.J. & Fleck N.A., 2001: Numerical analysis of strain gradient effects in periodic media. *Journal De Physique IV*, 11, 153–160.
- Polhemus N.W., 2005: How to: Construct a control chart for autocorrelated data. StatPoint Technologies, Herndon, 16 p.
- Russo D. & Jury W.A., 1987: A theoretical study of the estimation of the correlation scale in spatially varied fields, 2. Nonstationary fields. *Water Resources Research*, 23, 1269–1279.
- Russo S.L., Camargo M.E. & Fabris J.P., 2012: Applications of control charts ARIMA for autocorrelated data. In: Nezhad M.S.F. (Ed.): Practical Concepts of Quality Control. InTech, Rijeka, 31–53 p. doi: 10.5772/S0990.
- Simon D. & Anderson M., 1990: Stability of clay minerals in acid. In: SPE Formation Damage Control Symposium. *Society of Petroleum Engineers*, SPE-19422-MS, doi: 10.2118/19422-MS.
- Soeder D.J., 1986: Laboratory drying procedures and the permeability of tight sandstone core. *SPE Formation Evaluation*, 1, 16–22.
- Tiab D. & Donaldson E., 1996: Petrophysics: Theory and Practice of Measuring Reservoir Rock and Fluid Properties. Gulf Publishing Company, Houston. 706 p.
- Van Geet M., Swennen R. & Wevers M., 2000: Quantitative analysis of reservoir rocks by microfocus X-ray computerised tomography. *Sedimentary Geology*, 132, 25–36.

- Varga A.R., Szakmány G.Y., Raucsik B. & Máthé Z., 2005: Chemical composition, provenance and early diagenetic processes of playa lake deposits from the Boda Siltstone Formation (Upper Permian), SW Hungary. *Acta Geologica Hungarica*, 48, 49–68.
- Varga A., Raucsik B., Szakmány G.Y. & Máthé Z., 2006: Mineralogical, petrological and geochemical characteristics of the siliciclastic rock types of Boda Siltstone Formation. *Bulletin of the Hungarian Geological Society*, 136, 2, 201–232
- Vogel H.J., Cousin I. & Roth, K., 2002: Quantification of pore structure and gas diffusion as a function of scale. *European Journal of Soil Science*, 53, 3, 465–473.
- Webster R., 2000: Is soil variation random? *Geoderma*, 97, 149–163.
- Wesolowski J.R. & Lev H.M., 2005: CT: History, technology, and clinical aspects. *Seminars in Ultrasound, CT and MRI*, 26, 376–379.
- Withers P.J., Bouman C., Carmignato S., Cnudde V., Grimaldi D., Hagen C.K., Eric Maire E., Manley M., Plessis A. & Stock S., 2021: X-ray Computed Tomography. *Nature Reviews Methods Primers*, 1, 18, 1–21. doi:10.1038/s43586-021-00015-4.
- Yang Y., Li Y., Yao J., Zhang K., Iglauer K., Luquot L. & Wang Z., 2019: Formation damage evaluation of a sandstone reservoir via pore-scale X-ray computed tomography analysis. *Journal of Petroleum Science and Engineering*, 183, 106356. doi.org/10.1016/j.petrol.2019.106356.
- Zhang D.X., Zhang R.Y., Chen S.Y. & Soll V.E., 2000: Pore scale study of flow in porous media: scale dependency, REV, and statistical REV. *Geophysical Research Letters*, 27, 8, 1195–1198.
- Zhou Z., Gunter, W. & Jonasson R., 1995: Controlling formation damage using clay stabilizers: a review. In: Annual Technical Meeting. *Petroleum Society of Canada, PETSOC*, 95–71. doi: 10.2118/95-71.